Cyclic plasticity of polycrystalline nickel under axial–torsional loading

N.R. Batane[a], D.J. Morrison[b,*], J.C. Moosbrugger[b]

[a] Department of Mechanical Engineering, University of Botswana, Gaborone, Botswana
[b] Department of Mechanical and Aeronautical Engineering, Clarkson University, Potsdam, NY 13699-5725, USA

A B S T R A C T

The axial–torsional cyclic deformation behavior of polycrystalline nickel was investigated by performing fully reversed plastic strain amplitude controlled fatigue experiments at effective plastic strain amplitudes ranging from 1×10^{-4} to 1×10^{-3}. Experiments were accomplished under proportional and 90° out-of-phase nonproportional loading paths. Results indicate that loading path has very little effect on the cyclic response at the lower effective plastic strain amplitude. However, at the higher effective plastic strain amplitude, significant additional hardening is induced by the nonproportional loading path.

Keywords:
Fatigue
Cyclic plasticity
Nickel
Biaxial loading

1. Introduction

During the past few decades, a great deal of research has been accomplished on the uniaxial cyclic plasticity of metals [1–9]. Far less work has been reported on multiaxial cyclic loading even though service conditions frequently involve this type of loading. Under axial–torsional cyclic loading conditions employing sinusoidal strain or load control histories, the mechanical response depends not only on the magnitudes of the applied axial and torsional loads, but also on the phase angle between the axial and torsional components [10–15]. During in-phase (proportional) loading, the orientations of the principal stress and strain axes remain fixed with respect to the specimen axes. However, during out-of-phase (nonproportional) loading, the principal axes of stress and strain rotate during the loading cycle. It is well established that some metals exhibit significantly greater cyclic hardening under nonproportional loading than under proportional loading. This phenomenon has been attributed to the additional slip systems that are activated during nonproportional loading and the resulting hardening effect of the dislocation interactions [11,14]. The maximum additional cyclic hardening caused by nonproportional loading usually occurs when the axial and torsional components are 90° out-of-phase [15].

Doong et al. [16] demonstrated that stacking fault energy has a significant influence on the additional hardening caused by nonproportional loading. They performed axial–torsional fatigue tests on 1100 aluminum, OFHC copper, and 310 stainless steel; which have respectively, high, medium, and low stacking fault energies. The amount of additional nonproportional hardening was inversely related to the magnitude of the stacking fault energy, owing to the influence that stacking fault energy has on cross-slip [16–19]. Cross-slip of screw dislocations occurs much easier in high stacking fault energy materials because of the smaller separation distance between the partial dislocation components. In aluminum, nearly identical cell dislocation structures are produced under proportional and nonproportional loading over a fairly wide range of plastic strain amplitudes. The ease of cross-slip enables slip on multiple slip planes regardless of the loading mode [16]. As a result, aluminum exhibits very little additional nonproportional hardening. Stainless steel, on the other hand, exhibits significantly different dislocation structures depending on the loading mode. Under proportional loading, slip is primarily confined to a single slip plane and causes the formation of highly planar arrays of dislocations. Under nonproportional loading, slip occurs on multiple slip planes and causes the formation of multiple slip dislocation structures such as cells and labyrinths [16]. Therefore, stainless steel exhibits a great deal of additional nonproportional hardening over a wide range of plastic strain amplitudes. For copper, which has a stacking fault energy intermediate between aluminum and stainless steel, proportional loading at low plastic strain amplitude produces single slip dislocation structures such as loop patches and persistent slip bands; whereas at high plastic strain amplitude, multiple slip structures such as cells and labyrinths form. Under nonproportional loading, dislocation cells form at plastic strain amplitudes as low as 8×10^{-5}, although the cell boundaries consist of rather diffuse arrays of dislocations. At higher plastic

* Corresponding author at: Department of Mechanical and Aeronautical Engineering, 8 Clarkson Avenue, Clarkson University, Potsdam, NY 13699-5725, USA. Tel.: +1 315 268 6585; fax: +1 315 268 6695.
E-mail address: dmorriso@clarkson.edu (D.J. Morrison).

Table 1
Nomenclature list.

Total axial strain: ε	Shear modulus: G
Total torsional shear strain: γ	Plastic axial strain: $\varepsilon_p = \varepsilon - \sigma/E$
Axial normal stress: σ	Plastic shear strain: $\gamma_p = \gamma - \tau/G$
Torsional shear stress: τ	Plastic axial strain amplitude: $\varepsilon_{pa} = (\varepsilon_{p,max} - \varepsilon_{p,min})/2$
Young's modulus: E	Plastic shear strain amplitude: $\gamma_{pa} = (\gamma_{p,max} - \gamma_{p,min})/2$

strain amplitude, the cell walls are very distinct and the cell diameters are smaller than those that form under proportional loading [16]. As a result, the amount of additional nonproportional hardening in copper depends on the magnitude of the plastic strain amplitude. Clavel and Feaugas [19] proposed that the maximum additional hardening in copper should occur at intermediate strain amplitudes where persistent slip bands form under proportional loading, but a well-defined cell structure forms under nonproportional loading. Zhang and Jiang [20] observed very little additional hardening in copper at plastic strain amplitudes on the order of 10^{-4}, but the additional hardening increased as plastic strain amplitude increased.

Most studies on the effects of loading mode on cyclic hardening have been accomplished on complex alloys, especially stainless steels. Relatively few studies on pure metals have been reported. As noted by Zhang and Jiang [20], microstructural features such as precipitates and twins, as well as phenomena such as stress-induced phase transformations, can influence loading mode effects in alloys. These influences make it difficult to identify the contributions from the various cyclic plasticity mechanisms. Therefore, the objective of the present work was to provide additional insight into fundamental cyclic plasticity behavior by performing axial–torsional cyclic deformation experiments on pure polycrystalline nickel. To the authors' knowledge, only one other study [21] has reported on the effects of loading mode on the cyclic response of pure nickel; and that study did not investigate the low amplitude response addressed here.

2. Experimental procedures

Thin-walled tubular axial–torsional specimens were machined from a 19 mm diameter Ni-270 rod (99.98% Ni). Each specimen had a gage section outside diameter of 12.15 mm, wall thickness of 1 mm, and gage section length of 15 mm. After machining, the specimens were annealed in a vacuum of 5×10^{-6} Torr for 1 h at 500 °C, resulting in a grain size of about 50 μm. The specimens were then electropolished in a solution of 100 ml perchloric acid and 400 ml ethanol. Optimum electropolishing results were obtained at 50 V and −50 °C. X-ray texture analysis revealed a weak {1 1 1} longitudinal texture.

Axial–torsional cyclic deformation experiments were performed at room temperature on an MTS 809 axial–torsional testing system. The tests were run under total strain control using sinusoidal command signals, but the axial and shear total strain amplitudes were continuously adjusted to achieve reasonably constant effective plastic strain amplitude and to maintain the ratio of the shear plastic strain amplitude to the axial plastic strain amplitude equal to the von Mises normalization factor of $\sqrt{3}$. Pertinent stress and strain parameters are defined in Table 1.

An automated MTS TestWare-SX program was used to control the test parameters and to digitally acquire data at specified intervals. Total axial strain, ε, was measured using an MTS clip-on extensometer; and total engineering shear strain, γ, was acquired by four precision strain gages bonded to the gage section of the specimen. Axial and torsional loads were measured using an MTS axial–torsional load cell. The experiments were carried out under both proportional and 90° out-of-phase nonproportional loading using conditions shown in Table 2. We shall refer to these two types of loading conditions as proportional and nonproportional loading. For the constant amplitude tests, the specimens were cycled at the indicated effective plastic strain amplitudes until the stress amplitudes had clearly saturated. For the multiple step tests, the specimens were cycled to saturation at sequentially increasing effective plastic strain amplitudes. All cycling was accomplished at a frequency less than 1 Hz, and hysteresis loops were recorded at 0.05 Hz. Following the method described by Jiang and Kurath [22], we define effective plastic strain amplitude, $\varepsilon_{pa,eff}$, as the radius of the circle that circumscribes the loading path in plastic strain space ($\gamma_p/\sqrt{3}$ *vs.* ε_p). For proportional loading, $\varepsilon_{pa,eff} = (\varepsilon_{pa}^2 + \gamma_{pa}^2/3)^{1/2}$; and for the nonproportional loading used in this study, we approximate the radius of the circular loading path as $\varepsilon_{pa,eff} = (\varepsilon_{pa} + \gamma_{pa}/\sqrt{3})/2$.

Table 2
Axial–torsional experimental conditions.

	Proportional	Nonproportional
Constant amplitude	$\varepsilon_{pa,eff} = 1 \times 10^{-4}$	$\varepsilon_{pa,eff} = 1 \times 10^{-4}$
Constant amplitude	$\varepsilon_{pa,eff} = 1 \times 10^{-3}$	$\varepsilon_{pa,eff} = 1 \times 10^{-3}$
Multiple step test	$\varepsilon_{pa,eff} = 1 \times 10^{-4}$–$1 \times 10^{-3}$	$\varepsilon_{pa,eff} = 1 \times 10^{-4}$–$1 \times 10^{-3}$

Brightfield TEM images of the specimens cycled to saturation at the constant effective plastic strain amplitudes were obtained using a JEOL 1200 EX microscope operating at 120 kV. TEM specimens were sectioned from the gage section so that the foil normal was parallel to the radial direction. TEM disks were electrolytically thinned in a solution of 500 ml methanol, 100 ml butoxyethanol, 11.2 g magnesium perchlorate, and 5.3 g lithium chloride. Optimum thinning was obtained at 45 mA and −35 °C.

3. Results and discussion

3.1. Axial–torsional stress–strain response

The axial–torsional stress–strain responses of specimens cycled to saturation at constant effective plastic strain amplitudes ($\varepsilon_{pa,eff} = 1 \times 10^{-4}$ and 1×10^{-3}) are shown in Figs. 1 and 2. These figures show the axial response (σ *vs.* ε_p) and von Mises normalized torsional response ($\sqrt{3}\tau$ *vs.* $\gamma_p/\sqrt{3}$) of each specimen. For the proportionally loaded specimens shown in Fig. 1, the axial and torsional responses at the same $\varepsilon_{pa,eff}$ are quite similar. The only notable difference is that at $\varepsilon_{pa,eff} = 1 \times 10^{-4}$, the axial mode experienced slightly more cyclic hardening than the torsional mode as shown in Fig. 1(a) and (b). Some of that difference can be accounted for by a slight undershooting of the torsional plastic strain amplitude. The magnetostriction-induced constriction of the hysteresis loop commonly seen in nickel uniaxially cycled at low plastic strain amplitude [23,24] is clearly seen in the $\varepsilon_{pa,eff} = 1 \times 10^{-4}$ loops shown in Fig. 1(a) and (b). The responses of the specimens cycled under nonproportional loading are shown in Fig. 2. As with the proportional specimens, the axial and torsional responses are quite similar. Rather than exhibiting a distinct peak and well-defined linear elastic unloading region, the loops are quite rounded. This observation is caused by the fact that during 90° out-of-phase nonproportional loading, the response does not follow a purely elastic unloading path in stress space.

The responses of the specimens cycled to saturation at constant $\varepsilon_{pa,eff}$ are plotted in plastic strain space ($\gamma_p/\sqrt{3}$ *vs.* ε_p) and stress space ($\sqrt{3}\tau$ *vs.* σ) in Figs. 3 and 4. Proportional loading causes the 45° line path and nonproportional loading causes the circular path. The plastic strain responses shown in Figs. 3(a) and 4(a) indicate that at both effective plastic strain amplitudes, the imposed plastic strain

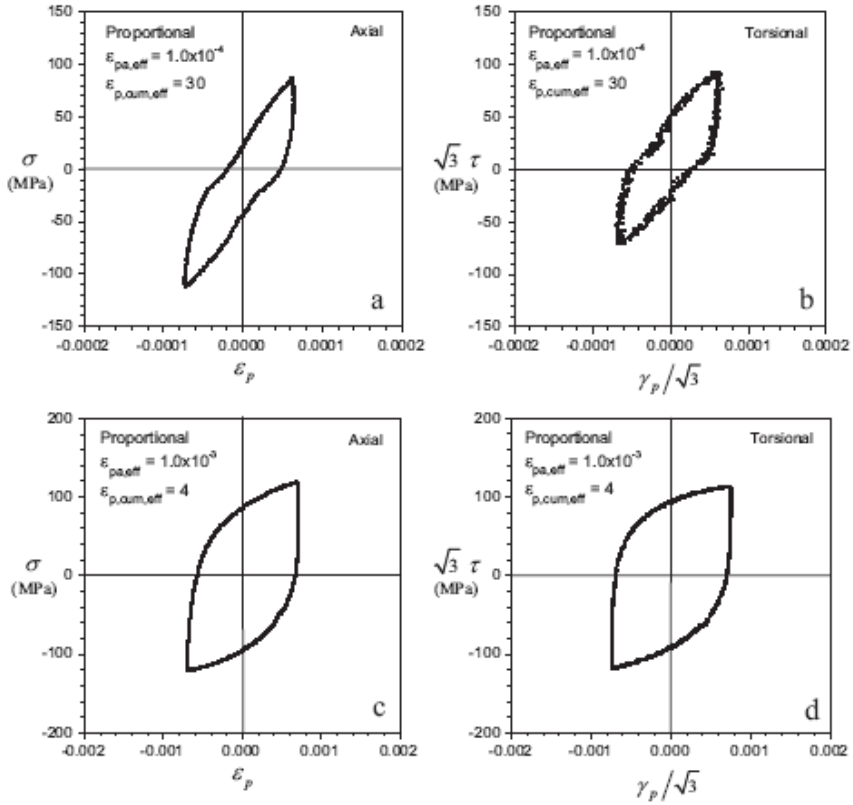

Fig. 1. Axial and torsional stress–strain responses at cyclic saturation for specimens cycled under proportional loading at $\varepsilon_{pa,eff} = 1 \times 10^{-4}$ (a) and (b) and $\varepsilon_{pa,eff} = 1 \times 10^{-3}$ (c) and (d).

path is quite close to the desired profile. Specifically, the nonproportional plastic strain path is nearly circular, the path is centered on the origin, and the radius is very close to the target effective plastic strain amplitude. Likewise, for the proportionally loaded specimens, the plastic strain path is a 45° line with minimal hysteresis, the line is centered on the origin, and the half-length of the line is very close to the target effective plastic strain amplitude. Ideally, the line should form the diameter of the circle described by the nonproportional loading. The resulting stress-space responses are shown in Figs. 3(b) and 4(b). The stress-space responses reflect the general features of the imposed plastic strain-space paths. For the nonproportionally loaded specimens, the stress-space responses are nearly circular and centered on the origin, although the circles are slightly elongated in the axial stress direction. For the proportionally loaded specimens, the stress-space responses are 45° lines. Fig. 3(b) shows that at $\varepsilon_{pa,eff} = 1 \times 10^{-4}$, the response is somewhat asymmetric with the line displaced upward and to the left of the origin. During plastic strain-controlled cyclic loading at low plastic strain amplitude, it is fairly common to see slight asymmetry in the stress response. Fig. 4(b) shows that at $\varepsilon_{pa,eff} = 1 \times 10^{-3}$, the proportional response is quite symmetric. For nonproportional loading, the mean radius of the circular loading path represents the effective stress amplitude, $\sigma_{a,eff}$. For proportional loading, $\sigma_{a,eff}$ is represented by one half the loading line length. A comparison of the stress responses in Figs. 3(b) and 4(b) indicates that at the lower strain amplitude, loading path has very little effect on $\sigma_{a,eff}$. However, at the higher strain amplitude, nonproportional loading causes a significantly higher $\sigma_{a,eff}$.

3.2. Axial–torsional cyclic hardening

Stress-space plots similar to those in Figs. 3(b) and 4(b) were obtained at periodic intervals during the constant amplitude tests. From these plots, $\sigma_{a,eff}$ was computed; and cyclic hardening curves were constructed that plot $\sigma_{a,eff}$ *vs.* $\varepsilon_{p,cum,eff}$ (cumulative effective plastic strain). Here, $\varepsilon_{p,cum,eff} = 4N\varepsilon_{pa,eff}$ where N is the number of cycles. The cyclic hardening curves are shown in Fig. 5. At $\varepsilon_{pa,eff} = 1 \times 10^{-4}$, nonproportional loading causes a significantly higher initial hardening rate, although the nonproportional and proportional specimens cyclically saturated at approximately the same $\sigma_{a,eff}$. At $\varepsilon_{pa,eff} = 1 \times 10^{-3}$, nonproportional loading causes a higher hardening rate and a significantly higher cyclic saturation $\sigma_{a,eff}$. From these cyclic hardening curves and from additional cyclic hardening information obtained during the multiple step tests, the cyclic stress–strain (CSS) curves shown in Fig. 6 were constructed. The CSS curve is a plot of the effective stress amplitude at saturation, $\sigma_{sa,eff}$, *vs.* the $\varepsilon_{pa,eff}$ at which the specimen was cycled. Fig. 6 shows that at low $\varepsilon_{pa,eff}$, loading path has very little influence on saturation stress. However, as $\varepsilon_{pa,eff}$ increases, the additional hardening caused by the nonproportional loading becomes quite pronounced. At $\varepsilon_{pa,eff} = 1 \times 10^{-3}$, the nonproportional strain path causes about a 28% increase in the saturation effective stress amplitude. This

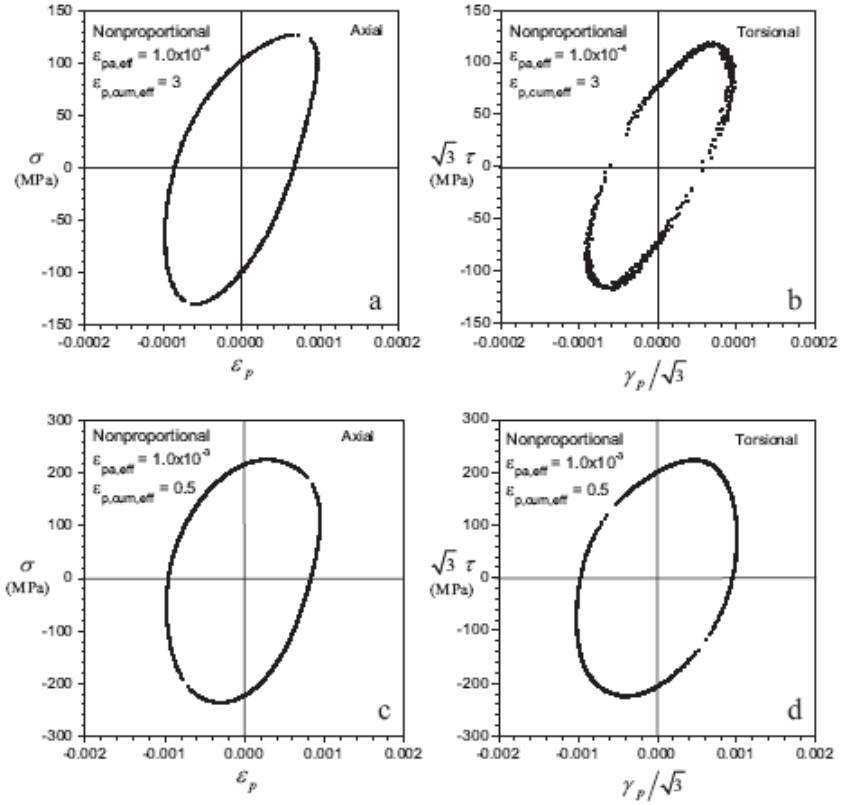

Fig. 2. Axial and torsional stress–strain responses at cyclic saturation for specimens cycled under nonproportional loading at $\varepsilon_{pa,eff} = 1 \times 10^{-4}$ (a) and (b) and $\varepsilon_{pa,eff} = 1 \times 10^{-3}$ (c) and (d).

compares favorably with a value of 27% reported by Itoh et al. [21] for nickel tested at $\varepsilon_{pa,eff} = 1 \times 10^{-3}$. As effective plastic strain amplitude decreases to 1×10^{-4}, the additional hardening diminishes to nearly zero. Zhang and Jiang [20] also noted a reduction of the additional nonproportional hardening in copper as effective plastic strain decreases. For comparison purposes, the CSS curve for uniaxially loaded polycrystalline nickel [25] is also shown in Fig. 6. The uniaxial results generally follow the proportional CSS curve, although at $\varepsilon_{pa,eff}$ between 1×10^{-4} and 3×10^{-4}, the uniaxial results are somewhat higher.

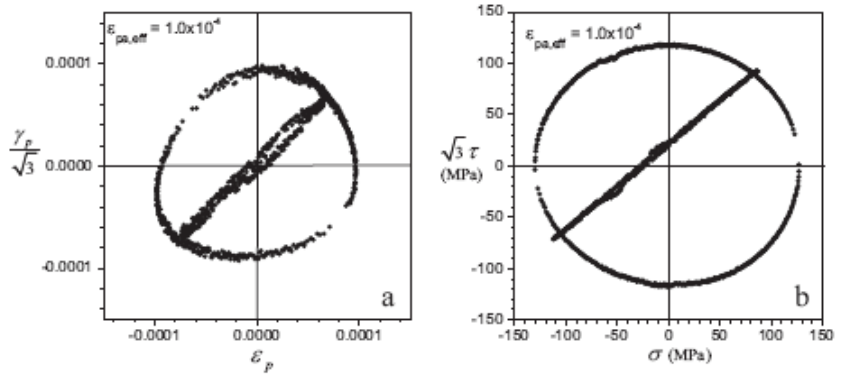

Fig. 3. Proportional and nonproportional plastic strain paths (a) and stress responses (b) for specimens cycled to saturation at $\varepsilon_{pa,eff} = 1 \times 10^{-4}$.

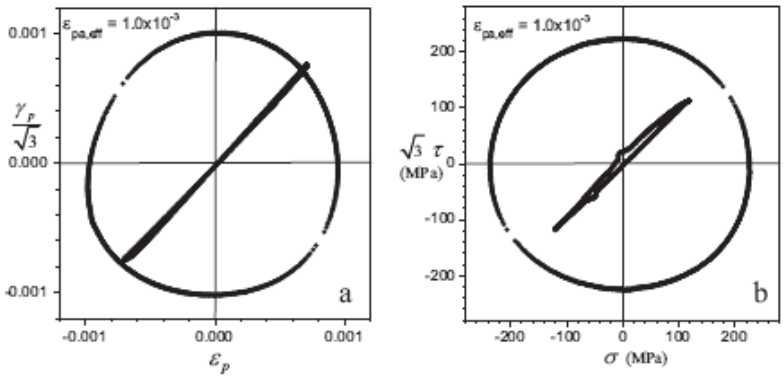

Fig. 4. Proportional and nonproportional plastic strain paths (a) and stress responses (b) for specimens cycled to saturation at $\varepsilon_{pa,eff} = 1 \times 10^{-3}$.

3.3. Transmission electron microscopy

Transmission electron micrographs of the cyclically saturated specimens are shown in Fig. 7. All the micrographs have the same orientation as given by the arrows in Fig. 7(b) indicating the longitudinal (L) and circumferential (C) directions. Dislocation structures produced in specimens cycled at $\varepsilon_{pa,eff} = 1 \times 10^{-4}$ are shown in Fig. 7(a) (proportional) and (b) (nonproportional). For both loading paths, the dislocation structure consists of high dislocation density loop patches separated by relatively dislocation-free channels. This type of dislocation structure is commonly seen in nickel cycled uniaxially at low plastic strain amplitude and is usually referred to as the vein structure [25–27]. The similar dislocation structures in the proportional and nonproportional specimens cycled at the lower effective plastic strain amplitude account for the nearly identical saturation effective stress amplitudes. The fact that the nonproportional specimen hardened much more rapidly indicates that nonproportional loading probably causes a more rapid evolution of the dislocation structure. However, pre-saturation TEM images would be required to confirm that speculation. The vein dislocation structure is usually associated with single slip behavior. However, it has been demonstrated that the vein structure can contain a significant content of secondary dislocations [28,29]. Therefore, it is possible that the vein dislocation structure can accommodate multiple slip induced by nonproportional loading when the strain amplitude is low.

Dislocation structures formed in the specimens cycled at $\varepsilon_{pa,eff} = 1 \times 10^{-3}$ are shown in Fig. 7(c) (proportional) and (d) (nonproportional). Fig. 7(c) shows that the proportional loading path produces persistent slip bands embedded in a matrix of the vein structure, similar to the type of structure formed in nickel cycled uniaxially at intermediate plastic strain amplitudes [25–27]. Under nonproportional loading at $\varepsilon_{pa,eff} = 1 \times 10^{-3}$, a cell dislocation structure is formed as shown in Fig. 7(d). This type of dislocation structure is associated with multiple slip conditions [25–27]. The significantly different dislocation structures cause the differences in both the hardening rate and saturation effective stress amplitudes.

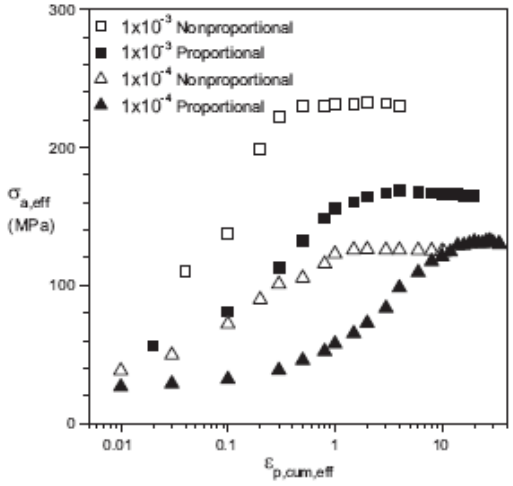

Fig. 5. Cyclic hardening curves for proportional and nonproportional specimens cycled at $\varepsilon_{pa,eff} = 1 \times 10^{-4}$ and $\varepsilon_{pa,eff} = 1 \times 10^{-3}$.

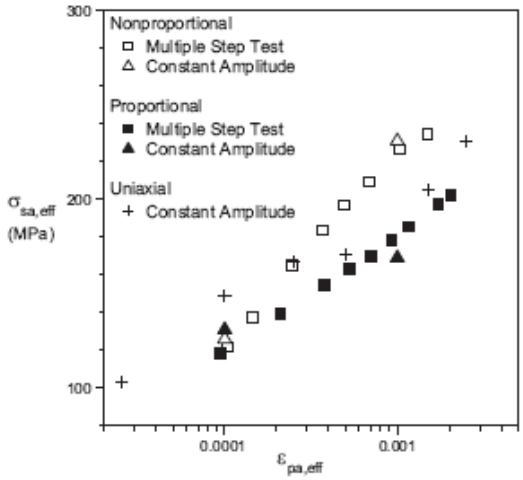

Fig. 6. Cyclic stress–strain curves for proportional and nonproportional specimens. Data for uniaxially loaded nickel are also shown.

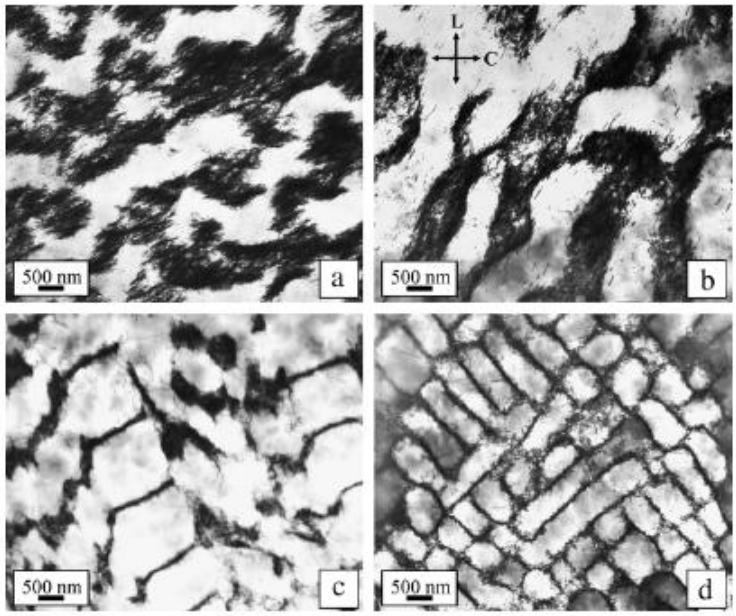

Fig. 7. Brightfield TEM images of saturation dislocation structures. (a) Proportional, $\varepsilon_{pa,eff} = 1 \times 10^{-4}$, (b) nonproportional, $\varepsilon_{pa,eff} = 1 \times 10^{-4}$, (c) proportional, $\varepsilon_{pa,eff} = 1 \times 10^{-3}$ and (d) nonproportional, $\varepsilon_{pa,eff} = 1 \times 10^{-3}$.

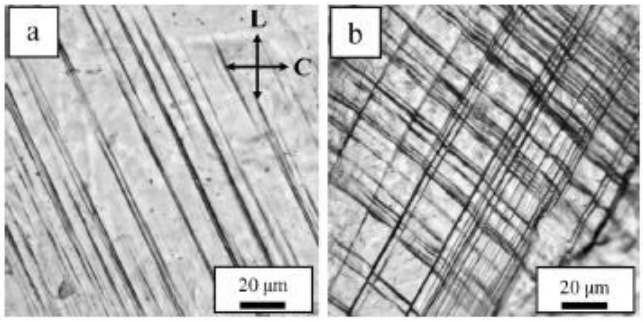

Fig. 8. Optical micrographs of acetate replicas extracted from the surfaces of specimens cycled at $\varepsilon_{pa,eff} = 1 \times 10^{-3}$ under (a) proportional and (b) nonproportional loading.

3.4. Surface slip features

Analyses of the surface slip features generally reflect the results of the TEM observations. The surfaces of the specimens cycled under both loading paths at $\varepsilon_{pa,eff} = 1 \times 10^{-4}$ were virtually featureless. Some large grains contained one or two parallel slip traces, but there was no evidence of intersecting slip traces that would indicate the activation of multiple slip systems. At $\varepsilon_{pa,eff} = 1 \times 10^{-3}$, the situation was quite different. Fig. 8(a) and (b) shows optical micrographs of acetate replicas extracted from the surfaces of specimens cycled at $\varepsilon_{pa,eff} = 1 \times 10^{-3}$ under proportional and nonproportional loading, respectively. The orientations of the micrographs are the same and given by the arrows in Fig. 8(a). Slip traces were especially common in larger grains. As shown in Fig. 8(a), proportional loading caused the formation of one set of parallel slip traces. However, under nonproportional loading, larger grains contained at least two sets of pronounced intersecting slip traces as shown in Fig. 8(b). Clearly, nonproportional loading at the higher effective plastic strain amplitude activated multiple slip systems.

4. Conclusions

From the results of this study on the axial–torsional cyclic plasticity of polycrystalline nickel, the following conclusions are made:

1. When cycled at low effective plastic strain amplitude ($\varepsilon_{pa,eff} = 1 \times 10^{-4}$), the initial cyclic hardening rate is higher under nonproportional loading. However, loading path has very little influence on the cyclic saturation effective stress. Saturation dislocation structures for both proportionally and nonproportionally loaded specimens consist primarily of the vein structure.
2. Loading path has a significant effect on the cyclic response at high effective plastic strain amplitude ($\varepsilon_{pa,eff} = 1 \times 10^{-3}$). Nonpropor-

tional loading causes a higher hardening rate and saturation effective stress amplitude owing to the activation of multiple slip systems. Saturation dislocation structures in proportionally loaded specimens consist of persistent slip bands embedded in a matrix of the vein structure. Nonproportionally loaded specimens consist of well-defined dislocation cells.

3. The effects of axial–torsional loading path on the low and high strain amplitude responses of nickel correlate very well with copper results previously reported by Zhang and Jiang [20]. This observation broadens previously noted similarities in the uniaxial cyclic plasticity of these metals [30]. In addition, the high strain amplitude results agree with similar experiments on nickel accomplished by Itoh et al. [21].

Acknowledgements

The authors gratefully acknowledge the support of the National Science Foundation through grant CMS 0201487. Support for axial–torsional testing facilities was provided by the National Science Foundation through grant CMS-9512140. N. Batane acknowledges the generous support of the University of Botswana.

References

[1] P. Lukas, M. Klesnil, J. Krejci, Phys. Status Solidi 27 (1968) 545–558.
[2] H. Mughrabi, Mater. Sci. Eng. 33 (1978) 207–223.
[3] C. Blochwitz, U. Veit, Cryst. Res. Technol. 17 (1982) 529–551.
[4] C. Laird, L. Buchinger, Metall. Trans. A 16A (1985) 2201–2214.
[5] C. Laird, P. Charsley, H. Mughrabi, Mater. Sci. Eng. 81 (1986) 433–450.
[6] J. Polak, J. Helesic, K. Obrtlik, Mater. Sci. Eng. A 101 (1988) 7–12.
[7] Z.S. Basinski, S.J. Basinski, Prog. Mater. Sci. 36 (1992) 89–148.
[8] O.B. Pedersen, A.T. Winter, Phys. Status Solidi A 149 (1995) 281–296.
[9] P. Lukas, L. Kunz, Philos. Mag. 84 (2004) 317–330.
[10] H.S. Lamba, O.M. Sidebottom, ASME J. Eng. Mater. Technol. 100 (1978) 96–103.
[11] K. Kanazawa, K.J. Miller, M.W. Brown, Fatigue Eng. Mater. Struct. 2 (1979) 217–228.
[12] E. Krempl, H. Lu, ASME J. Eng. Mater. Technol. 106 (1984) 376–382.
[13] E. Tanaka, S. Murakami, M. Ooka, J. Mech. Phys. Solids 33 (1986) 559–575.
[14] D.L. McDowell, D.R. Stahl, S.R. Stock, S.D. Antolovich, Metall. Trans. 19A (1988) 1277.
[15] A. Benallal, P. Le Gallo, D. Marquis, D. Nucl. Eng. Des. 114 (1989) 345–353.
[16] S.H. Doong, D.F. Socie, I.M. Robertson, ASME J. Eng. Mater. Technol. 112 (1990) 456.
[17] F.R.N. Nabarro, Adv. Phys. Suppl. Philos. Mag. 1 (1952) 269.
[18] M.V. Borodii, S.M. Shukaev, Int. J. Fatigue 29 (2007) 1184–1191.
[19] M. Clavel, X. Feaugas, in: A. Pineau, G. Cailletaud, T.C. Lindley (Eds.), Multiaxial Fatigue, Design, ESIS 21, Mechanical Engineering Publications, London, 1996, pp. 21–41.
[20] J. Zhang, Y. Jiang, Int. J. Plasticity 21 (2005) 2191–2211.
[21] T. Itoh, M. Sakane, M.K. Ohnami, K. Ameyama, Proceedings of Mecamat 92, International Seminar on Multiaxial Plasticity, LMT-Cachan, France, 1992, pp. 43–50.
[22] Y. Jiang, P. Kurath, Int. J. Plasticity 13 (1997) 743.
[23] D.J. Morrison, Y. Jia, J.C. Moosbrugger, Scr. Mater. 44 (2001) 449–453.
[24] Y. Jia, D.J. Morrison, J.C. Moosbrugger, Scr. Mater. 53 (2005) 1025–1029.
[25] D.J. Morrison, Mater. Sci. Eng. A 187 (1994) 11–21.
[26] D.J. Morrison, V. Chopra, Mater. Sci. Eng. A 177 (1994) 29–42.
[27] C. Buque, J. Bretschneider, A. Schwab, C. Holste, Mater. Sci. Eng. A 300 (2001) 254–262.
[28] F. Ackermann, L.P. Kubin, J. Lepinoux, H. Mughrabi, Acta Metall. 32 (1984) 715–725.
[29] L. Llanes, A.D. Rollett, C. Laird, J.L. Bassani, Acta Metall. Mater. 41 (1993) 2667–2679.
[30] H. Mughrabi, F. Ackermann, K. Herz, in: J.T. Fong (Ed.), Proc. ASTM-NBS-NSF Symp. ASTM Spec. Tech. Publ. 675, American Society for Testing and Materials, Philadelphia, PA, 1979, pp. 69–105.